Journal of Power Sources 632 (2025) 236296

Contents lists available at ScienceDirect

Journal of Power Sources

journal homepage: www.elsevier.com/locate/jpowsour

# Steam and polarization effects on Ni-YSZ electrode due to degradation under electrolysis and fuel cell operation

Aiswarya Krishnakumar Padinjarethil [a,1], Fiammetta Rita Bianchi [b,*], Anke Hagen [a], Barbara Bosio [b]

[a] Department of Energy Conversion and Storage, Technical University of Denmark (DTU), Building 310, Fysikvej, DK-2800, Lyngby, Denmark
[b] Department of Civil, Chemical and Environmental Engineering (DICCA), University of Genova, Via Opera Pia 15, 16145, Genova, Italy

## HIGHLIGHTS

- Ni instability leads to significant penalization of solid oxide cell performance.
- Ni migration prevails under electrolysis mode due to high local potentials.
- Ni coarsening characterises fuel cell mode combining steam and load effects.
- Water content and applied current density are Ni degradation driving forces.

## GRAPHICAL ABSTRACT

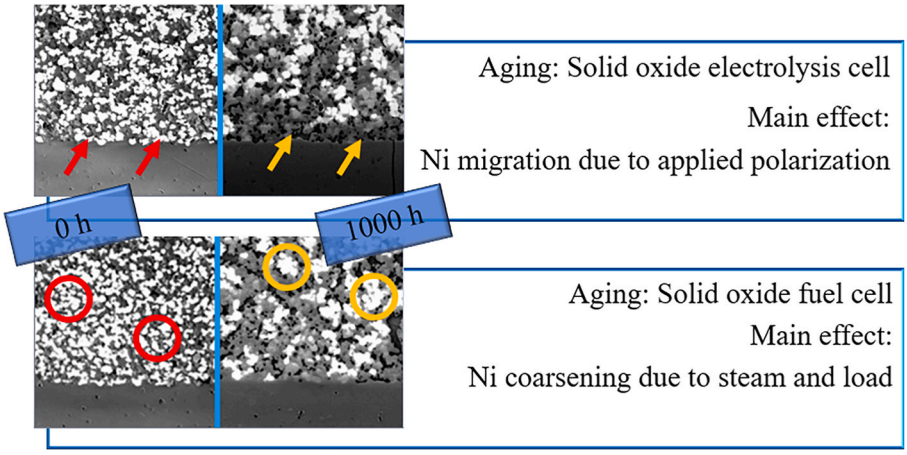


## ARTICLE INFO

*Keywords:*
Solid oxide cell
Steam electrolysis
Fuel cell
Ni-cermet degradation
Multiscale modelling

## ABSTRACT

Degradation issues correlated to microstructural changes are the main obstacles to solid oxide fuel cell and electrolyser applications, making their identification and understanding fundamental steps. Coupling experimental activities with modelling, this work analyses the state-of-the-art Ni-YSZ (Yttria-Stabilized Zirconia)/YSZ/CGO (Cerium Gadolinium Oxide)/LSCF (Lanthanum Strontium Cobalt Ferrite)-CGO-based cell after 1000 h of galvanostatic electrolysis operation at fixed temperature and high steam composition in the inlet gas. Following a multiscale approach, the system behaviour is characterized through electrochemical impedance spectra and polarization curves as well as studying microstructure evolution, with a focus on Ni-cermet functional layer in view of Ni instability detected as the main degradation cause. A comparison with a cell consisting of the same initial geometrical structure and materials but aged in fuel cell mode allows to highlight the influence of operating mode and parameters on Ni-YSZ microstructure. Ni particle size and phase fraction variations experimentally observed on the electrode surface are correlated to water content and applied polarization

* Corresponding author.
*E-mail address:* fiammettarita.bianchi@unige.it (F.R. Bianchi).
[1] Topsoe A/S, Haldor Topsøes Allé 1, Kongens Lyngby, 2800, Denmark.

https://doi.org/10.1016/j.jpowsour.2025.236296
Received 26 February 2024; Received in revised form 12 August 2024; Accepted 20 January 2025
Available online 31 January 2025

simulated local values. Ni uneven distribution at the electrolyte interface and particle coarsening, above all, lead to an increase in polarization loss under electrolysis and fuel cell mode, respectively, since both penalise the charge transfer reaction and migration.

## 1. Introduction

Solid Oxide Cells (SOCs) are an emerging energy conversion technology in view of their high performance as co-generation systems and electrolysers coupled with renewables. High temperatures (usually above 700 °C) are required for the operation of Solid Oxide Fuel Cell (SOFC) to provide both electricity and heat and of Solid Oxide Electrolysis Cell (SOEC) to favour water dissociation supplying electric energy and heat [1,2]. Despite several promising prototypes at the system level and initial commercial applications [3–6], SOCs are still not competitive in the energy market in view of their limited lifetime of around 45,000 h and 10,000 h operation for fuel cell and electrolysis modes, respectively [7]. The performance loss is mainly due to microstructural variations, which characterize multi-layer ceramic materials at high temperatures, such as element migration and secondary phase formation [8]. In this framework the hydrogen electrode, usually consisting of a Ni cermet, is widely recognized as one of the main degradation sources [9]. Ni use allows for high catalytic activity of $H_2$ redox reactions as well as for good electronic conductivity [10], but the risk of Ni migration and particle agglomeration is frequent under the desired working conditions [11]. Furthermore, the manufacturing process has a significant impact on the microstructure evolution: fine or coarse initial particles show different coarsening rates and the specific ratio of the ceramic phase to the Ni phase can hinder Ni mobility and change the reaction site number [12,13].

Several studies have tested solid oxide cells at different sets of working conditions and operation times. The humidity level is typically concluded to be a severe degradation cause since it enhances both Ni migration and coarsening mechanisms [14]. Indeed, at high temperatures, 20 % moisture is sufficient to form stable volatile species, above all $Ni(OH)_2$, resulting in Ni re-localization [15]. The main consequences are already visible in SOFC working at high fuel utilizations [16], but they are more pronounced under the electrolysis mode due to a higher fed steam content [17]. It was observed that Ni particle agglomeration causes significant changes even after a few hundred working hours [18–20]. Referring specifically to Ni-YSZ cermet used commonly at the commercial level, quite asymptotic growth is detected due to the YSZ backbone inhibiting effect if its volumetric fraction is sufficient to guarantee a good, percolated network [21]. For instance, after more than 4400 h SOEC operation feeding 90 vol% of water, the cell showed significant performance changes mainly concentrated in the initial 250 h, resulting in a global degradation rate of 25 mV per 1000 h due to the loss of Ni-Ni grain contacts as well as Ni-YSZ grain contacts within the functional layer [22]. Testing 50 vol% $H_2O$ feed, this lower steam content was still sufficient to provoke Ni diffusion from the active zone, resulting in Ni enrichment of the support layer compared to the virgin structure [23]. Indeed, Ni usually migrates away from the electrode-electrolyte interface to reach a more stable status [24]. The applied polarization has also a significant impact on Ni-cermet degradation processes in both fuel cell and electrolysis modes, favouring Ni mobility. As a function of the electrode microstructure and the impurity level, there is an overpotential threshold value (around 160–300 mV) to avoid complete Ni depletion near the electrolyte according to the previous literature [25].

In such a framework, this work discusses Ni-YSZ/YSZ/CGO/LSCF-CGO cell durability under electrolysis and fuel cell operation. It is mainly devoted to Ni-YSZ analysis in view of the high Ni instability, which makes the hydrogen electrode a significant degradation source. The reported observations aim at overcoming the existent literature gap, where a direct comparison between two operation modes is quite challenging in view of different tested sample structures and working point sets, highlighting the role of inlet gas composition and applied load on the cell degradation. Based on the authors' previous studies on solid oxide fuel cell behaviour before and after aging [26,27], the same approach was followed in the first part of the present work to characterize the electrolyser long-term degradation. Then, considering both cell operation modes, the local changes of the material properties detected by the post-mortem microstructural analysis were correlated to the measured pre- and post-electrochemical performances through the kinetics modelling, providing a clear cause-and-effect explanation of the main observed degradation mechanisms.

## 2. Methods

### 2.1. Experimental setup

A hydrogen electrode-supported cell was tested under long-term electrolysis operation to evaluate its performance and degradation. It consists of a Ni-YSZ hydrogen electrode, which serves both as the support and the functional layer (~250 μm), a dense YSZ electrolyte (8–10 μm), a CGO thin barrier layer (2–5 μm) to avoid secondary phase formation and an LSCF-CGO air composite electrode (~50 μm). Cells were laser cut into 5.3 cm × 5.3 cm with a resulting active area of 16 $cm^2$ for the testing sample. The electrolysis durability test was carried out with an $H_2$ flow of 1 l $h^{-1}$ and $H_2O$ of 12 l $h^{-1}$ (produced by the previous combustion of inlet $H_2$ and $O_2$), resulting in around a 10/90 vol% $H_2$/$H_2O$ ratio on the fuel side, and a flow of 63 l $h^{-1}$ dry air on the air side. The cell was operated for 1000 h under a galvanostatic operation with a current density of −0.4 A $cm^{-2}$ at 750 °C (steam utilization of ~22 %). The conditions for the aged fuel cell taken as the reference for Ni-YSZ degradation consisted of 1000 h feeding a 96/4 vol% $H_2$/$H_2O$ anodic mixture and dry air as the oxidant at 750 °C and 0.4 A $cm^{-2}$ (hydrogen utilization of ~14 %), as described in detail in the authors' previous devoted work [27]. It is noteworthy that the applied load in the electrolysis mode is lower than the target commercial values; nevertheless, it was chosen to be equal to the fuel cell mode one (usually working at lower current densities) to analyse the operation mode impact on the cell degradation, removing the effects due to different loads.

The cells were studied under long-term operation as well as during pre- and post-electrochemical characterisation through Electrochemical Impedance Spectroscopy (EIS) analysis and polarization curve measurements ("fingerprint" at variable temperatures, loads, hydrogen/steam ratios and oxidant contents). In addition (Fig. 1), the microstructural qualitative-quantitative analysis was performed on reduced virgin samples and aged samples cut from the inlet and the outlet cell sections in order to highlight specific local variations.

The spectra were recorded by a Solartron frequency analyser, monitoring between 96 kHz and 0.08 Hz with 12 points per decade with integration over 100 measurements to ensure good quality data. After checking the individual spectra through linearised Kramer Kronig tests, they were analysed by a suitable Equivalent Circuit Model (ECM) and Complex Nonlinear Least Squares (CNLS) fitting. ECM consists of an inductance element in series with an ohmic resistor, four sub-circuits built up of a resistor and a constant phase element in parallel, and a single Gerisher element. For the microstructural characterization, Scanning Electron Microscopy (SEM) imaging was carried out on 1 cm × 1 cm cut samples. The procedures were described in more detail in the authors' previous works. Briefly, for quantification purposes using the in-home software ManSeg, more than 1000 particles of each sample were taken to ensure an error lower than 5 % for the different phases

(specifically <2 % referring to percolating Ni) [26,28].

### 2.2. Multiscale modelling

SIMFC/SIMEC (SIMulation of Fuel Cells and Electrolysis Cells) is an in-home 2D Fortran code, built at the University of Genoa, to simulate high-temperature cell behaviour by solving conservation equations on the cell plane through a finite difference approach [29–32]. It allows modelling the global performance starting from an ad hoc electrochemical formulation dependent on the computed local working conditions and the imposed uneven distributions of microstructural features. Here it forecasts the electrochemical behaviour by plotting polarization curves and the most significant physicochemical properties, such as the current density, the gas composition and the overpotentials, in terms of their local distributions on the anodic and cathodic planes as well as their global values as an average. In detail, assuming an isopotential cell plane, the voltage is evaluated as the algebraic sum of the Nernst equilibrium value and a series of polarization losses derived from Ohm law and Butler-Volmer equation. The ohmic overpotential depends on the temperature following an Arrhenius-type formulation; the activation overpotential is influenced by the temperature and the fed gas composition through a semi-empirical formulation of the exchange current density; finally, the diffusion overpotential considers the limiting current density of the main reactant (i.e., hydrogen in fuel cell mode and water in electrolysis mode) computing its average partial pressure along the electrode thickness. With the aim of studying Ni-cermet-based electrode degradation [8,33], its physicochemical properties are formulated as a function of the structural parameters following the percolation theory [34]. Table 1 reports a summary of the main equations (refer to the authors' previous works for the complete model description [27,35,36]). Note that an isothermal behaviour was here assumed in view of the small size of the cell and the proper thermal management of the test house. Input data are the feed conditions and some intrinsic cell properties, which were retrieved by experimental observations: the microstructure features, such as particle radii and phase fractions, were computed by SEM image analysis, while the kinetic parameters in terms of activation energies and reactant kinetic orders derived from ECM analysis on EIS spectra. A 10 x 10 mesh was applied for simulation purposes.

As the performance indexes, the absolute and relative degradation rates are evaluated. The absolute degradation rate, $DR_{abs}$, computes the $x$-variable (i.e., cell voltage and resistances) absolute variation over the considered time $t$ (eqn (1)), whereas the relative degradation rate $DR\%$ normalises this difference on the initial value (eqn (2)). In both cases, 1000 h are commonly assumed as the reference time.

$$DR_{abs} = |x_t - x_0|1000 / t \quad (1)$$

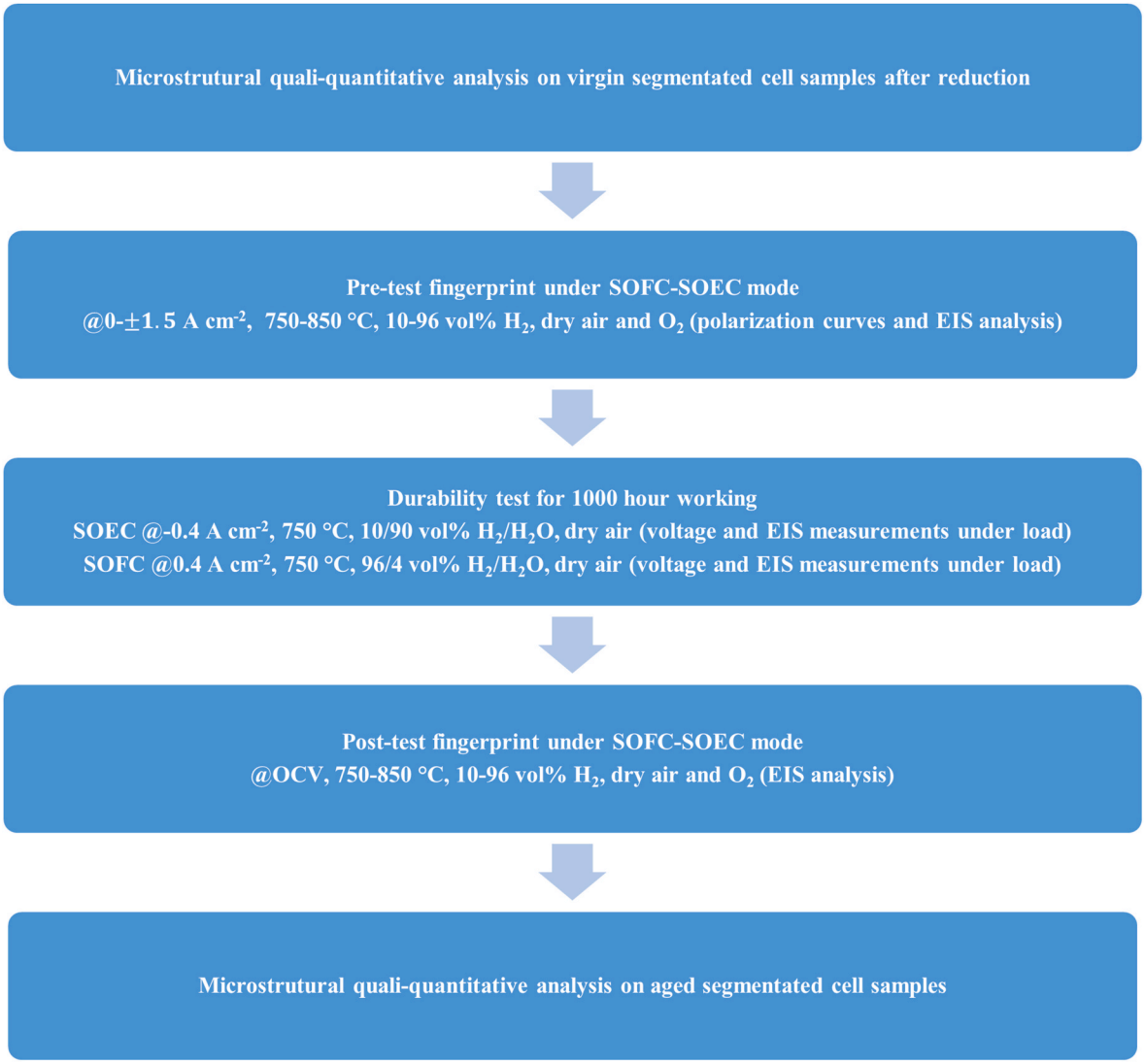


**Fig. 1.** Solid oxide cell test consisting of microstructural and electrochemical characterization.

**Table 1**
Electrochemical kinetics formulation for Ni-cermet based solid oxide cell in SIMFC/SIMEC model.

| | |
|---|---|
| **Material balances on the cell plane** | $\frac{\partial N_{i,j}}{\partial X_j} = \frac{\nu_i J_j}{zF}$ and $\frac{\partial N_{i,j}}{\partial Y_j} = \frac{\nu_i J_j}{zF}$ $\forall$ *i-th* component in each *j-th* sub-cell |
| **Cell voltage** | $V_{cell} = E_{av}^{eq} \pm \sum \eta_{av}$ (each term derived from local value average) |
| **Polarization losses** | $\eta_{ohmj} = R_{ohmj} J_j = \left[ \gamma_{ohmj} T \exp\left( \frac{E_{act,ohm}}{R_g T} \right) \right] J_j$ in each *j-th* sub-cell |
| | $\eta_{actj} = \frac{2R_g T}{zF} \sinh^{-1} \left[ \frac{J_j}{2\gamma_j \prod y_{i,j}^{\alpha_i} \exp\left( \frac{-E_{act}}{R_g T} \right)} \right]$ $\forall$ electrode in each *j-th* sub-cell |
| | $\eta_{diff} = \left\lvert \frac{R_g T}{zF} \ln\left( 1 - \frac{J_j}{J_{\lim\ -i,j}} \right)^{2\alpha_i} \right\rvert$ $\forall$ electrode in each *j-th* sub-cell |
| **Ni-YSZ physicochemical features** | $R_{ohmj} = \frac{d}{\sigma_{Ni,j} + \sigma_{YSZ,j}}$ where $\sigma_{n,j}^{eff} = \sigma_{n,0} (1-\varepsilon_j)^2 \left[ \frac{\Psi_{n,j} - \Psi_{n,j}^t}{1 - \Psi_{n,j}^t (1-\varepsilon_j)} \right]^2$ $\forall$ *n-th* phase |
| | $\gamma_j = \gamma' l_{TPB}^{eff} j$ in each *j-th* sub-cell where $l_{TPB}^{eff} j = \frac{3(1-\varepsilon_j)\Psi_{Ni,j}}{4\pi r_{Ni}^3 j} \left[ \pi \sin\theta \min\left( r_{Ni,j}, r_{YSZ,j} \right) \right] \frac{\left( 1 + \frac{r_{Ni}^2 j}{r_{YSZ,j}^2} \right) 6\Psi_{YSZ,j} r_{Ni,j}}{\Psi_{YSZ,j} r_{Ni,j} + \Psi_{Ni,j} r_{YSZ,j}} p_{TPB}^{Ni} j p_{TPB}^{YSZ} j$ |

**List of symbols**: *d*: Electrode thickness, $E^{eq}$: Open circuit voltage, $E_{act}$: Activation energy, *F*: Faraday constant, *J*: Current density, $J_{lim}$: Limiting current density, $l_{TPB}$: Triple phase boundary density, *N*: Linear flow rate, $p_{TPB}$: Particle probability of belonging to percolating network, $R_g$: Ideal gas constant, $R_{ohm}$: Ohmic resistance, *r*: Particle radius, *T*: Temperature, *V:* Voltage, *X-Y*: Spatial coordinates, *y*: Molar fraction, *z*: Charge number, $\alpha$: Reactant kinetic order, $\gamma$ and $\gamma'$: Kinetic constants, $\varepsilon$: Porosity, $\eta$: Overpotential, $\nu$: Stochiometric coefficient, $\theta$: Contact angle between cermet particles, $\sigma$: Conductivity, $\Psi$: Solid phase fraction.

$$DR_{\%} = \left( \left| \frac{x_t - x_0}{x_0} \right| 1000 \Big/ t \right) 100\% \quad (2)$$

## 3. Results

SOEC performance degradation was evaluated starting from the experimental observations derived from voltage response and EIS spectra recorded during the durability test in addition to the pre- and post-durability electrochemical characterization at different feed compositions and temperatures under both OCV (Open Circuit Voltage) and an external applied load. Post-mortem microstructural analysis of virgin and aged cut samples allowed the identification of possible sources for the observed voltage increase. Finally, the cell local modelling was used to create a link between the variations of voltage and resistances measured at the macroscale level and the material aging observed at the microscale level.

### 3.1. Electrolysis durability test and electrochemical characterization

During the durability test under a galvanostatic operation, the electrolyser voltage shows a continuous increase except for an interruption after 150 h of operation due to technical reasons (Fig. 2A). It is noteworthy that such a profile was post-experiment corrected by removing the leak effects due to the break (refer to Supplementary Material and Figure S1 for more details). Quite high voltage degradation rates are detected with a rapid rise in the first working hours to finally obtain ~3.5 V% $kh^{-1}$ after 1000 h of operation. This value is quite comparable by order of magnitude with the previous literature works, where a range of 2–10 V% $kh^{-1}$ has been reported for solid oxide electrolysis cells [37]. For instance, an averaged value of ~4.6 V% $kh^{-1}$ was obtained under −1 A $cm^{-2}$ and 800 °C feeding a 10/90 vol% $H_2/H_2O$ mixture [22]. At 850 °C the voltage degradation rate exceeded ~9 V% $kh^{-1}$ after 1500 working hours at −0.5 A $cm^{-2}$ [13]. Working temperature effects were underlined in Refs. [38,39], where higher degradation rates characterised both 800 °C and 700 °C with fewer changes at intermediate values. A degradation rate of ~9.7 V% $kh^{-1}$ was also measured after just 250 h at 700 °C and −0.6 A $cm^{-2}$ under 50/50$H_2/H_2O$ vol% feed [40]. Knowing Ni-YSZ instability, infiltrated electrodes were also recently tested showing ~2 V% $kh^{-1}$ at −1.25 A $cm^{-2}$ and 750 °C after 800 h [41].

Looking at the resistances derived from EIS analysis along the test duration (Fig. 2B), they were less influenced by the current interruption showing a minimum variation correlated to a transient phase of the working conditions that had to be restabilized. The ohmic term is quite stable, whereas the polarization contribution increases continuously following an asymptotic profile with a fixed value after ~800 h. The total absolute degradation rate for the polarization resistance is 54 mΩ $cm^2$ $kh^{-1}$, which can be split as 98 mΩ $cm^2$ $kh^{-1}$ before 500 h and 8 mΩ $cm^2$ $kh^{-1}$ between 500 h and 1000 h. These preliminary observations suggest that the degradation should be mainly correlated to the electrodes with quite stable features of the electrolyte, since the ohmic resistance depends above all on the ion conduction. Referring to the Bode plots to have more insights, the main variations are visible at high frequencies that could be due to the degradation of the hydrogen electrode catalytic activity, usually detecting the Ni-YSZ charge transfer at around 2–6 kHz. The oxygen diffusion and surface kinetics in LSCF-CGO appear commonly at 0.1–1 kHz, showing minimum changes during the 1000 h tested SOEC operation [26,42–44]. Overlapping trends of low frequencies at the test start and end exclude significant effects on the gas transport processes. Quite similar considerations are obtained referring to EIS spectra recorded during the pre- and post-durability fingerprints (Figure S2).

### 3.2. Microstructural post-mortem analysis

A detailed microstructure investigation was performed from a qualitative and quantitative point of view to detect the main effects of electrolysis aging. The percolation imaging technique through in-lens secondary electron detector allowed a clear distinction between the percolating Ni (bright phase) from the non- or less percolating phases (dark phases). The virgin cell was analysed after its reduction under 5 vol% $H_2$ in $N_2$ at 750 °C. The sample shows good adhesion between all the different layers (Fig. 3A) and the cermet particles are observed to be homogeneously distributed in the Ni-YSZ electrode. After 1000 electrolysis working hours (Fig. 3B), neither detachment nor void formation within the electrolyte are visible, as suggested by a minimum variation of the ohmic resistance value (Fig. 2B). The oxygen electrode shows qualitatively only small changes, which can be correlated to Sr mobility as observed in previous studies on similar cells [45,46]. It is noteworthy that LSCF-CGO good stability derives from testing a single cell, since high-quality air was fed and there was no poisoning from interconnects as in the case of stacks [47,48]. Therefore, the following discussion

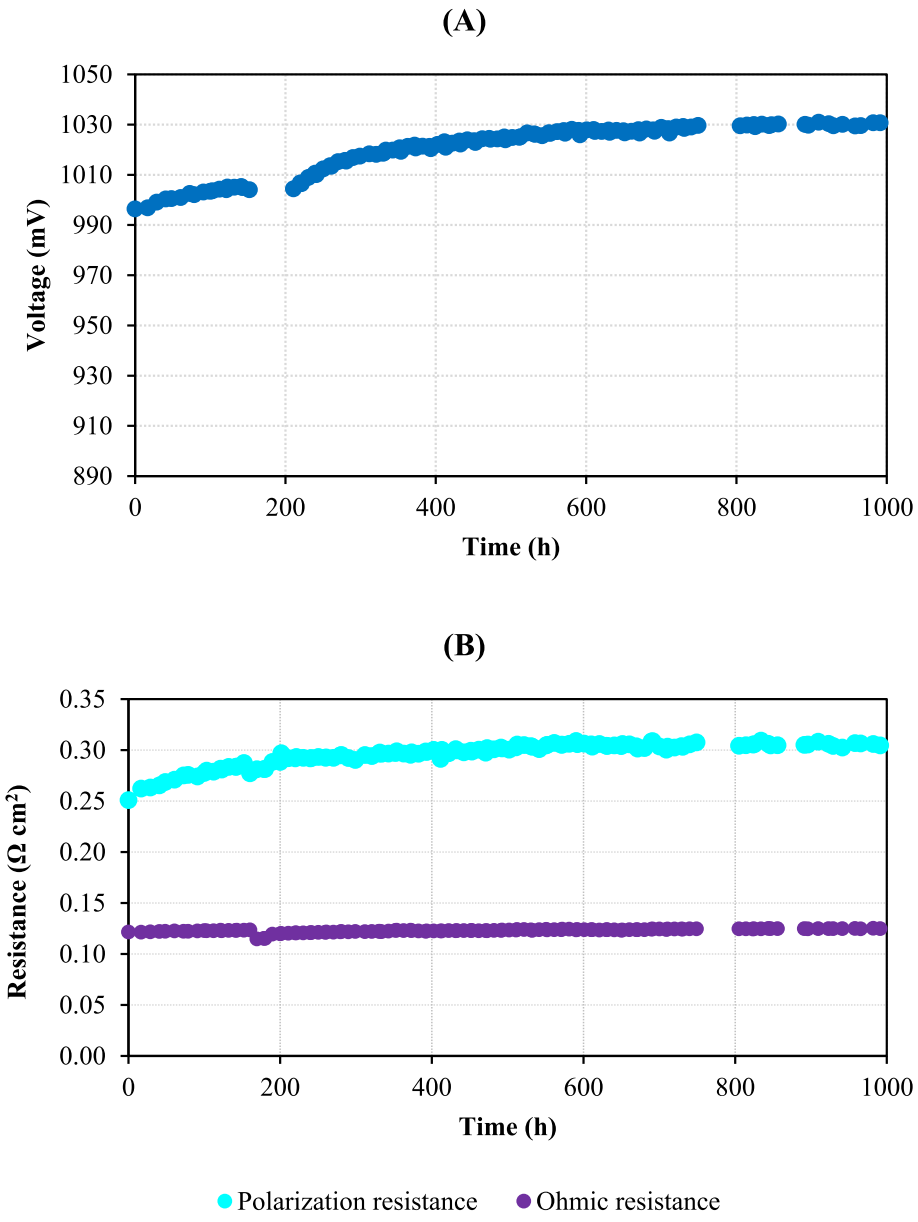


**Fig. 2.** Cell voltage (A), ohmic and polarization resistances determined by EIS analysis (B) during operation over 1000 h SOEC working at −0.4 A $cm^{-2}$ and 750 °C feeding 10/90 vol% $H_2/H_2O$ mixture and dry air.

focuses just on the hydrogen electrode which is the main cause of the performance drop, as reported in Refs. [9,22,33]. The cell was imaged using an in-lens secondary electron detector to identify the percolating Ni (bright spots) and the non-percolating Ni (dark spots) in the cermet. In the virgin sample, the percolating Ni is uniformly distributed across the hydrogen electrode (Fig. 3C); while in the aged cell the Ni particles of the functional layer (~10–15 μm) are larger in size as compared to the virgin one at both the inlet and the outlet sections (Fig. 3D and Figure S3). In addition, there is a Ni loss provoking a decrease in the percolating network due to its migration in ~2–5 μm thickness from the electrolyte interface to the electrode bulk, where a combination of Ni re-deposition and agglomeration increases the particle size [17,25,47,49]. All these phenomena result in a significant penalization of the hydrogen electrode polarization [19]. Previous studies have also shown the ohmic resistance rise due to the extension of $O^{2-}$ transfer distance to the reaction sites [19,22,50]. However, this phenomenon is not here observed (Fig. 2B), since only a fraction of the percolating Ni migrates away from the electrolyte-electrode interface, conserving the electrode network for the charge migration.

The quantitative analysis on the Ni-YSZ electrode was performed by ImageJ and ManSeg [51,52]. After aging the Ni particle size increases by ~20 %, resulting in similar values at the inlet and the outlet (Table 2). Consequently, the pore diameter reaches ~0.5 μm with respect to the initial ~0.3 μm size. Ni coarsening and migration cause the percolating network partial destruction, above all in the inlet section. Here the percolating Ni fraction reduces up to 0.17 (vs. 0.40 before testing), causing an increase in the porosity and the non-percolating Ni fraction (0.24 and 0.14 after testing vs. 0.15 and 0.05 before testing, respectively). The YSZ forms a quite stable backbone with minimum microstructural variations, mainly correlated to 2D image analysis limitations. However, considering the used percolation imaging technique for the post-mortem microstructural analysis, a maximum computation error of 5 % is detected on parameter identification in the case of dark phases (i.e., pore and YSZ), while a value lower than 2 % characterises the bright phase (i.e., percolating Ni) that can be easily identified. Thus, detected Ni migration and coarsening effects would be reliable.

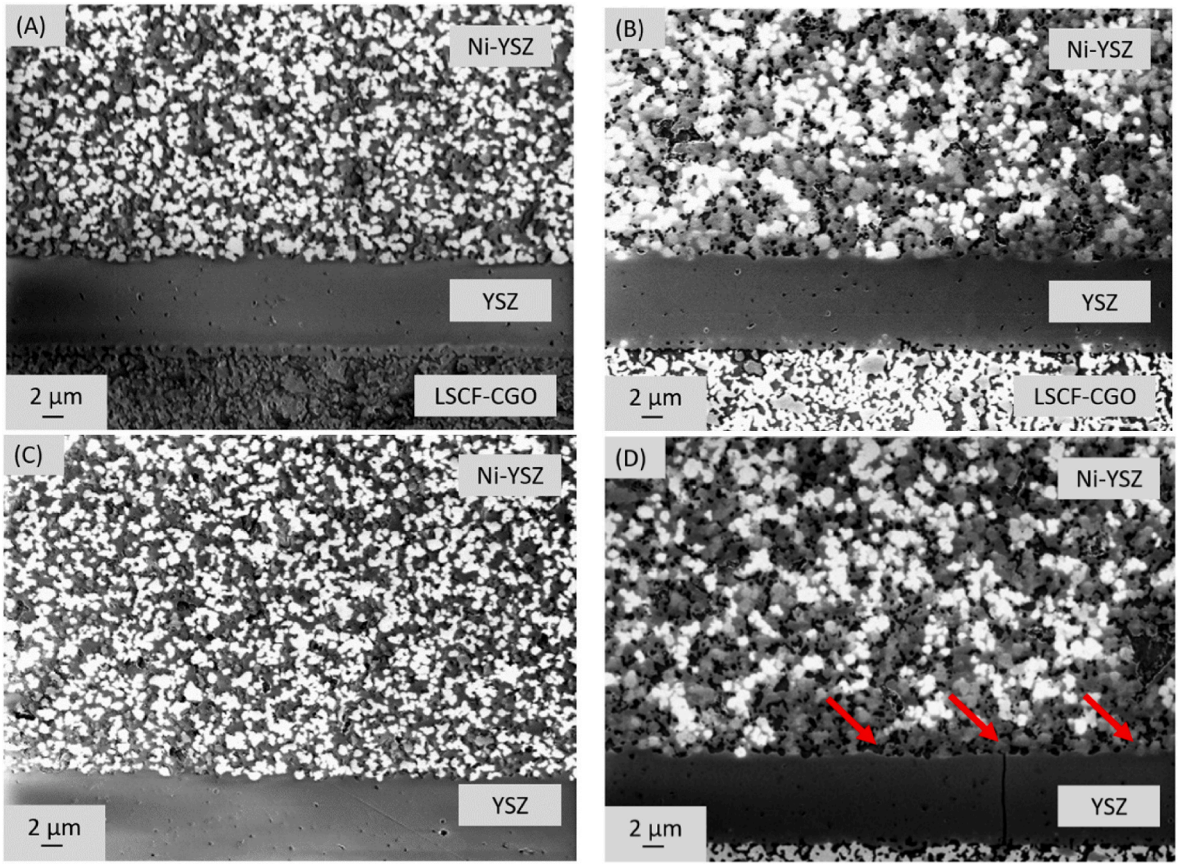


**Fig. 3.** SEM images of virgin reduced (A) and outlet aged (B) full cell, virgin (C) and inlet aged (D) Ni-YSZ active layer distinguishing pores (black), percolating Ni (bright), non-percolating Ni (light grey) and YSZ (dark grey). Red arrows in Figure (D) underline the percolating Ni partially depleted zone at the electrode-electrolyte interface due to Ni migration. (For interpretation of the references to colour in this figure legend, the reader is referred to the Web version of this article.)

**Table 2**
Post-mortem analysis of Ni-YSZ active layer by the comparison of electrolysis aging structure with respect to virgin one (computational error on parameter identification lower than 5 %).

| Parameter | Pre-durability | Post-durability | |
|---|---|---|---|
| | | Inlet | Outlet |
| Phase fraction (−) | | | |
| Pore | 0.15 | 0.24 | 0.20 |
| Percolating Ni | 0.40 | 0.17 | 0.20 |
| YSZ | 0.40 | 0.45 | 0.45 |
| Non-percolating Ni | 0.05 | 0.14 | 0.15 |
| Dimension (µm) | | | |
| Pore | 0.30 | 0.52 | 0.53 |
| Percolating Ni | 0.80 | 0.98 | 0.96 |
| YSZ | 0.60 | 0.60 (*) | 0.60 (*) |
| Non-percolating Ni | NA | 0.90 | 0.90 |

(*) supposed into the model based on known YSZ stability.

### 3.3. Cell kinetics modelling

A detailed comparison of the electrolysis cell operation between virgin cell and 1000 h aging status was performed through a physics-based modelling approach. The specific kinetic parameters for the Ni-YSZ/YSZ/CGO/LSCF-CGO cell derived from EIS analysis are reported in Table 3, referring to both pre- and post-durability cases (fitting errors lower than 1 %). Considering the pre-testing behaviour, the air electrode consisting of a perovskite-based composite layer has a higher activation energy compared to the Ni-YSZ hydrogen electrode [27,53]. Different kinetic orders for hydrogen and steam are evaluated to simulate the reversible cell operation, in view of their specific weight on the reaction path [54]. The oxygen kinetic order is lower confirming its minor influence, which is an LSCF peculiarity [55]. Analysing the aged cell spectra, no significant variation is detected for both kinetic orders and activation energies, which are assumed to be almost constant for pre- and post-durability performance simulation. Indeed, the degradation changes above all the pre-exponential coefficients of the exchange current density since they are correlated to the catalytic active site distribution. A higher variation of the hydrogen electrode coefficient is noteworthy (66 % Ni-YSZ vs. 37 % LSCF-CGO), explaining the high frequency process contribution increase. The ohmic parameters slightly vary, but they balance each other without causing a visible overall ohmic resistance rise (Fig. 2B).

**Table 3**
Kinetic parameters to simulate cell performance before and after 1000 h electrolysis working (fitting error on parameter identification lower than 1 %).

| Parameter | Pre-durability | Post-durability |
|---|---|---|
| Ohmic pre-exponential coef. ($\Omega$ cm$^2$ K$^{-1}$) | $5.9\bullet10^{-8}$ | $3.4\bullet10^{-8}$ |
| Ohmic activation energy (kJ mol$^{-1}$) | 64 | 70 |
| $H_2O$ kinetic order (−) | 1.08 | 1.08 |
| $H_2$ kinetic order (−) | 0.50 | 0.50 |
| Ni-YSZ activation energy (kJ mol$^{-1}$) | 107 | 105 |
| $O_2$ kinetic order (−) | 0.17 | 0.17 |
| LSCF-CGO activation energy (kJ mol$^{-1}$) | 120 | 120 |
| Ni-YSZ pre-exponential coef. (A cm$^{-2}$) | $1.2\bullet10^{6}$ | $4.1\bullet10^{5}$ |
| LSCF-CGO pre-exponential coef. (A cm$^{-2}$) | $8\bullet10^{5}$ | $5\bullet10^{5}$ |

Referring to Ni-YSZ microstructural parameters, the reduced sample has a homogeneous microstructure on the cell whole plane, which results in a TPB density of ~3.1 µm$^{-2}$ and a conductivity of ~970 S cm$^{-1}$ at 750 °C. Different local working conditions cause their uneven

distribution on the aged sample plane. Based on the post-mortem microstructural analysis, linear trends were assumed along the cathodic feed direction for Ni radius and phase fraction (Fig. 4A), creating their local maps to be applied as SIMFC/SIMEC model inputs. Such an assumption is justified by the quite small cell size and the reactant feeding design [31,56]. However, further studies on commercial-scale cells could apply a more detailed trend by diversifying the cut samples on the cell plane. The model allows for estimating the

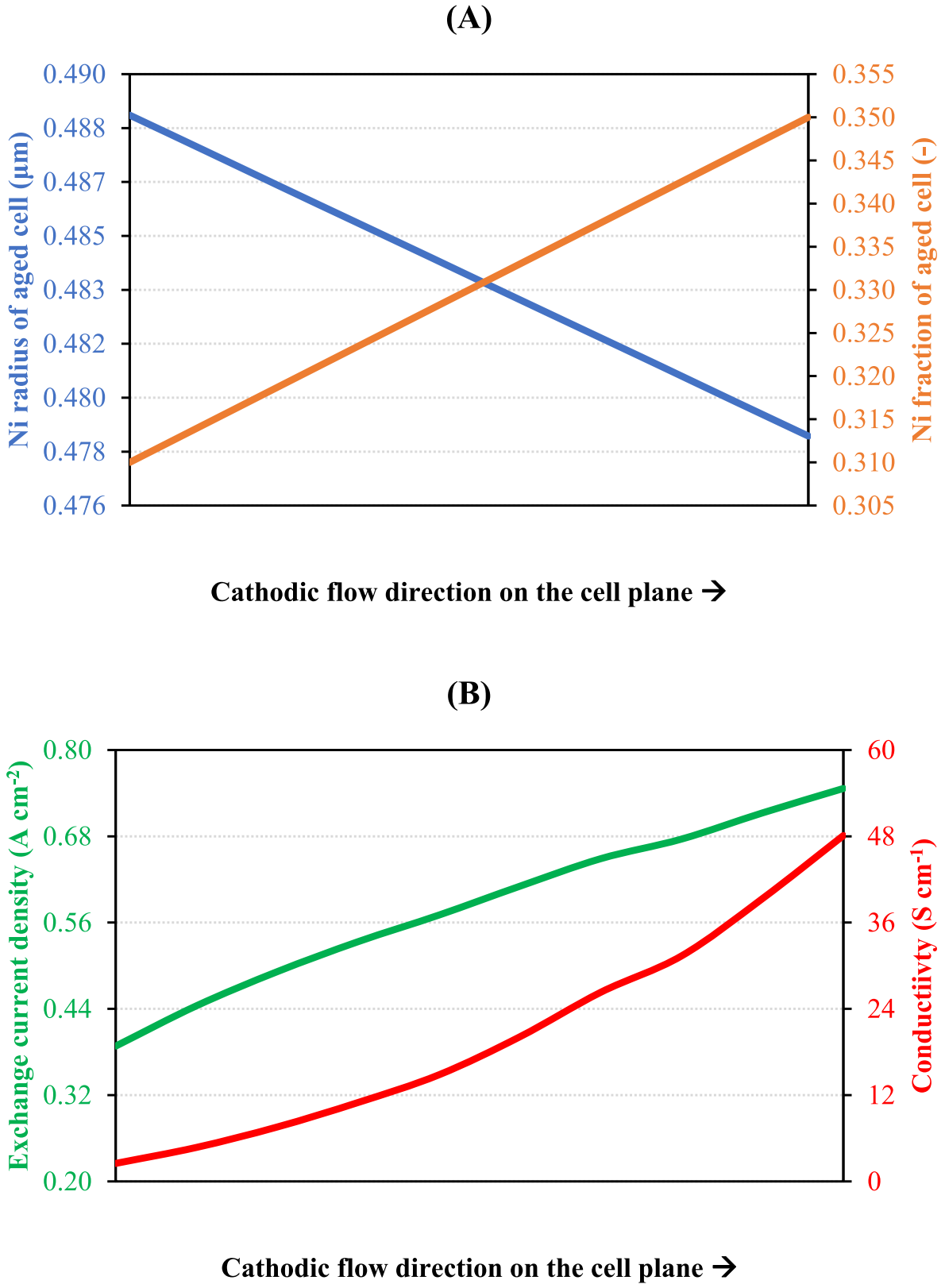


**Fig. 4.** Percolating Ni particle radius and Ni total phase fraction imposed linear increase on aged cell plane (A), allowing the calculation of exchange current density and conductivity for Ni-YSZ active layer (B) at OCV, 50/50 vol% $H_2/H_2O$, dry air and 750 °C by SIMFC/SIMEC.

attended local changes of the kinetic rate and the ohmic resistance in terms of the exchange current density (linearly increasing) and the cermet conductivity (almost exponentially increasing), respectively (Fig. 4B). Indeed, Ni-instability reduces (i) the TPB density due to a lower contact area between metal and ceramic particles, (ii) the charge migration in view of a lower Ni percentage at the electrolyte interface. The most severe effects occur at the inlet, where a higher Ni radius and a lower percolating Ni phase fraction are detected (Table 2). Variations of ~0.01 μm as Ni particle radius and ~0.04 percentage points as Ni total fraction between the cell extremities provoke an almost halved exchange current density value and a conductivity local variation of ~45 S $cm^{-1}$. However, the degradation processes mainly involve the activation overpotential and, to a lesser extent, the ohmic one. Indeed, the worsening of Ni-YSZ electrode conductivity leads to a minimum of ~2.5 S $cm^{-1}$ @750 °C, which is still two-orders of magnitude higher than the pure YSZ layer value (~0.03 S $cm^{-1}$ @750 °C). Since the electrolyte aging is negligible and the low Ni amount at the interface still allows a percolation network (Fig. 3), the ohmic overpotential did not increase under the testing period as previously observed for the same electrode configuration [19,57].

Basing on this local analysis, SIMFC/SIMEC model was first successfully validated by experimental data comparison referring to the fingerprints (relative error always lower than 4 % (Figure S4)). Then it was used to compare the reversible cell performance pre- and post-durability by simulating the characteristic curves (for example, pre- and post- IV curves under a 50/50 vol% $H_2/H_2O$ mixture and dry air in Fig. 5A and Figure S5, respectively). Referring to the overpotentials in fuel cell mode before aging (Figure S6), the combination of activation and ohmic terms has the highest impact except at high current densities. Whereas in electrolysis the diffusion loss plays a significant role also at low loads in view of a higher water molecular size compared to hydrogen. For example, considering the fuel cell working condition of 0.4 A $cm^{-2}$ (average value on the cell plane in SIMFC/SIMEC) at 750 °C, the ohmic and the activation contributions represent ~56 % and ~38 % of the total cell overpotential, respectively. The remaining ~6 % is covered by the diffusion term. In the electrolysis operation under −0.4 A $cm^{-2}$ (average value on the cell plane in SIMFC/SIMEC) and 750 °C, the ohmic and the activation overpotentials decrease at ~46 % and ~33 %, respectively, due to the ~21 % weight shown by the diffusion value. In the case of the aged cell (Figure S7), the main variation characterises the activation overpotential that becomes 47 % of the total losses in electrolysis mode (vs. 38 % and 15 % of the ohmic and diffusion terms, respectively) and 52 % of the total losses in fuel cell mode (vs. 44 % and 4 % of the ohmic and diffusion terms, respectively). This is above all due to Ni-YSZ functional layer degradation and only partly to the LSCF-CGO electrode. The voltage absolute degradation rate is finally used to

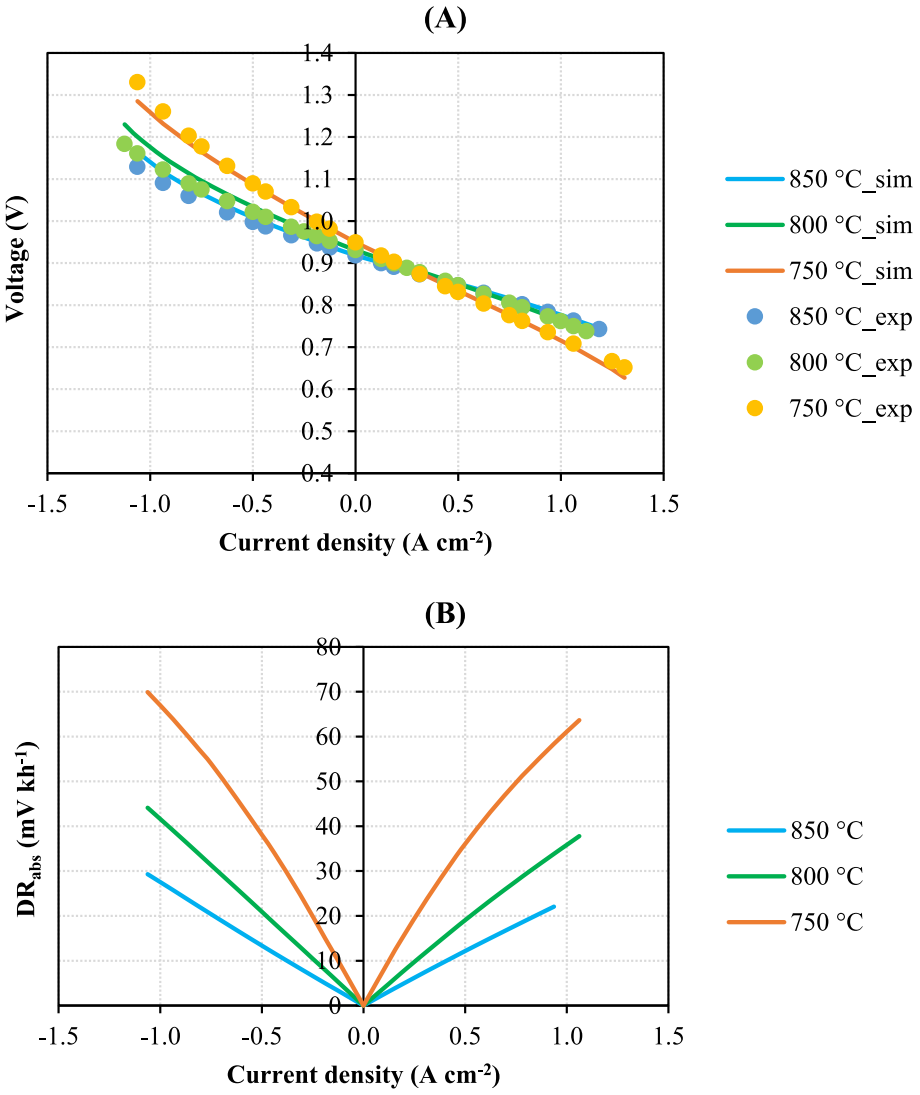


**Fig. 5.** IV curves for virgin cell performance (A) and absolute degradation rates after 1000 h aging (B) at 50/50 vol% $H_2/H_2O$ fuel and dry air under a reversible operation.

quantify the mismatch between pre- and post-testing IV curves (Fig. 5B). The curves at 750 °C present the worst performance, reaching a degradation rate of ~70 mV $kh^{-1}$ over −1 A $cm^{-2}$ in the electrolysis cell mode and of ~60 mV $kh^{-1}$ over 1 A $cm^{-2}$ in the fuel cell mode. At 850 °C and 800 °C the $DR_{abs}$ profiles are quite linear in view of the main weight shown by the ohmic losses. At 750 °C the activation overpotential is higher, explaining the visible asymptotic profile in accordance with the Butler-Volmer formulation [58].

## 4. Discussion

This section is devoted to underlining the peculiarities of Ni-YSZ degradation due to electrolysis and fuel cell operation: the first studied in detail in the present work, the second analysed in the authors' previous work [27]. It is noteworthy that the cell material and design are the same for both cases, allowing an effective comparison between their performances since the detected differences in aged samples are just due to specific working conditions.

Under a fuel cell operation, the cell showed a lower degradation rate (~0.6 V% $kh^{-1}$) with again a more significant change of the polarization resistance, which increased quite linearly (~12 % $kh^{-1}$) due to mainly the Ni-YSZ charge transfer process contribution. This was correlated to Ni-coarsening detected in the functional layer, which reduced the catalytic activity resulting in an activation overpotential increase.

### 4.1. Ni-YSZ degradation in terms of microstructural changes

Basing on SEM image analysis, the microstructural parameters of the Ni-YSZ functional layer were computed and compared in order to underline local differences between the degradation in fuel cell and in electrolysis operations (Fig. 6). The Ni/YSZ ratio is unitary in the virgin samples, confirming a homogenous distribution of metal and ceramic phases with a very low amount of non-percolating Ni. After 1000 working hours, the main visible changes are the percolating Ni fraction decrease (more accentuated after electrolysis operation) and the Ni particle size increase (more accentuated after fuel cell operation). Such aspects reduce the available Ni active surface, changing the percolation network of the Ni-YSZ electrode. Different local values are visible when comparing the inlet and outlet sections of the same aged sample as well. The electrolysis operation provokes a higher Ni migration (Fig. 6A),

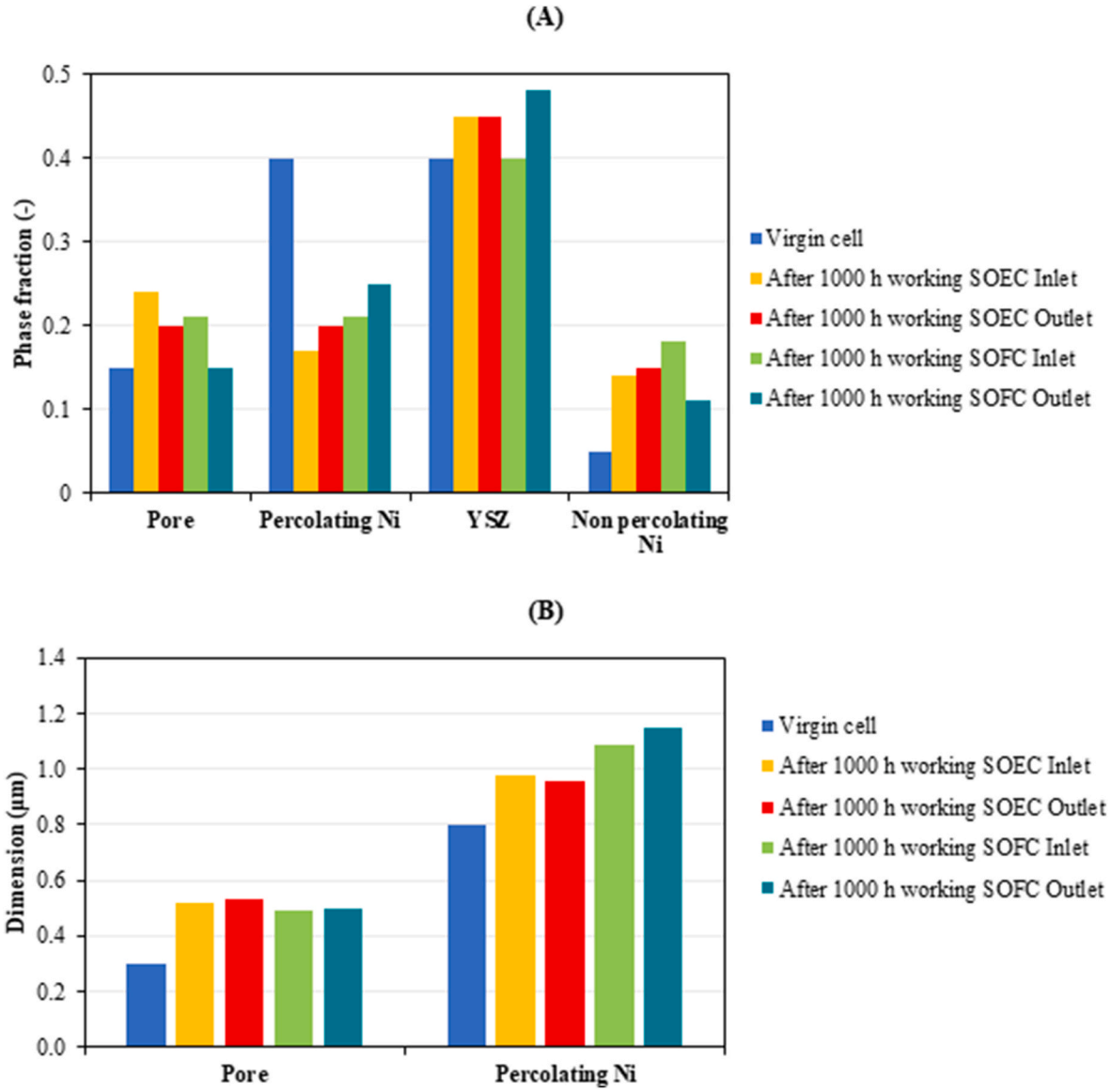


**Fig. 6.** Comparison of Ni-YSZ functional layer phase fractions (A), percolating Ni and pore sizes (B) after 1000 working hours in fuel cell and electrolysis mode at inlet and outlet sections with respect to virgin cell homogenous structure (computational error on parameter identification lower than 5 %).

leading to the minimum percolating Ni fraction of 0.17 (vs. 0.21 in fuel cell mode) and the maximum porosity of 0.24 (vs. 0.21 in fuel cell mode) at the inlet of the aged samples. In both cell operating modes, the percolating Ni fraction has an increasing trend following the gas flow direction and here it reaches the highest values at the outlet, the opposite for the porosity. Looking at the particle sizes (Fig. 6B), Ni agglomeration is detected in all the samples, but a higher radius characterises the cell tested in fuel cell mode obtaining a maximum increase of ~22 % and of ~44 % after electrolysis and fuel cell aging, respectively. In detail, the highest sizes correspond to the SOEC inlet section (0.98 μm) and to the SOFC outlet one (1.15 μm) in agreement with [12,49]. In the SOEC durability test, the local variation on the cell plane is quite negligible (i.e., a decrease of ~2 % between the inlet and the outlet), whereas the fuel cell aged sample shows bigger particles at the outlet with an increase of ~5 % with respect to the inlet value.

### 4.2. Ni-YSZ degradation due to local working conditions

The detected microstructure evolutions were explained by referring to local working conditions on the cell plane computed through SIMFC/SIMEC model. Indeed, experimental observations show a higher degradation at the cell inlet and at the cell outlet for the electrolysis and fuel cell aging, respectively. Several reference works have assumed the polarization as the possible driving force for Ni migration [16,59], which is confirmed in the present work. Indeed, the hydrogen electrode overpotential is higher at the SOEC inlet under the tested conditions of 10/90 vol% $H_2/H_2O$ fuel mixture and dry air at 750 °C and −0.4 A $cm^{-2}$ as an average current density on the cell plane. This is a consequence of higher local current densities (Fig. 7A) since the cell kinetics is favoured at the inlet where there are more reactants. The Ni-YSZ overpotential computed as the sum of activation and diffusion terms is 34 mV under an inlet local current density of −0.55 A $cm^{-2}$ and decreases at 17 mV under an outlet local value of −0.30 A $cm^{-2}$. Similarly, in fuel cell mode (96/4 vol% $H_2/H_2O$ fuel mixture and dry air at 750 °C and 0.4 A $cm^{-2}$ as an average current density on the cell plane), a higher local current density is computed at the inlet section characterised by a lower percolating Ni phase fraction (0.43 A $cm^{-2}$ at the inlet vs. 0.37 A $cm^{-2}$ at the outlet in Fig. 7B). Moreover, since the cell has an asymmetric electrochemical behaviour (Fig. 5A), under an equal absolute average value of 0.4 A $cm^{-2}$ Ni migration is more emphasized after electrolysis mode aging, which is characterised by higher polarization losses.

It is noteworthy that the present analysis was performed at working conditions more commonly used in solid oxide fuel cells but quite far from the commercial electrolyser target that overcomes −1 A $cm^{-2}$,

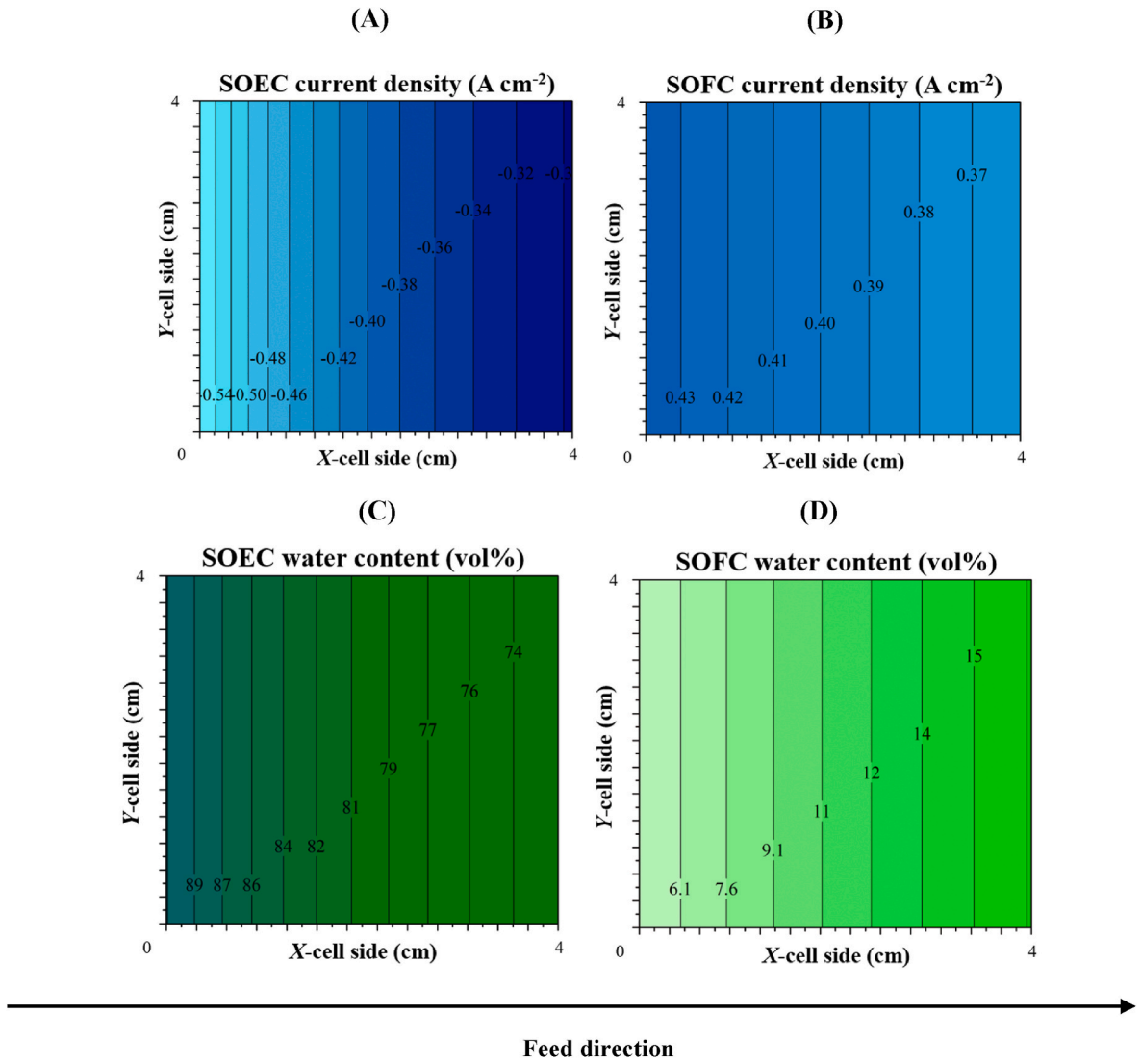


**Fig. 7.** Local maps of theoretical working conditions in terms of current density (A–B) and water volume fraction (C–D) under SOEC (A–C) and SOFC (B–C) operation according to SIMFC/SIMEC results (SOFC operation @0.4 A $cm^{-2}$ feeding 96/4 vol% $H_2/H_2O$ mixture and dry air at 750 °C, SOEC operation @-0.4 A $cm^{-2}$ feeding 10/90 vol% $H_2/H_2O$ mixture and dry air at 750 °C).

resulting in a more stressful operation and Ni migration enhancement. According to SIMFC/SIMEC model, the increase in applied average load causes higher local values on the cell plane, computing an increment as an absolute value up to ~0.15–0.16 A $cm^{-2}$ more. Here the Ni-YSZ overpotential also results higher looking at the local maps. For instance (Figure S8), at the reference working condition of 10/90 vol% $H_2/H_2O$ fuel mixture and dry air at 750 °C, an applied average current density of −0.8 A $cm^{-2}$ means an electrode overpotential of ~60 mV which overcomes ~100 mV over −1.4 A $cm^{-2}$ (with respect to ~34 mV @-0.4 A $cm^{-2}$). Here, in view of the polarizationdriving effect for Ni mobility, a more severe degradation should occur as observed in Refs. [11,60]. Moreover, higher applied loads can also activate further processes within the electrolysis cell, undermining electrolyte and oxygen electrode stability [61–63].

According to the previous literature, the particle agglomeration is above all dependent on the temperature firstly and the humidity level secondly [14,64]. Since a good thermal control was guaranteed in the furnace in view of the small cell dimension, the main difference on the cell plane involves the steam content and the applied current density resulting in both degradation-accelerating agents [65]. The water produced by SOFC leads to its fraction increase along the flow direction (Fig. 7D), which may explain the highest measured Ni size at the fuel cell outlet. In electrolysis operation, bit larger particles are reached at the inlet (i.e., 90 vol% $H_2O$) with respect to the outlet section (Fig. 7C). For the sake of clarity, a gas leak was detected during the electrolysis durability test; here the theoretical simulated local values of water content could be actually a bit underestimated. The steam content would seem to have a significant influence on the particle sintering, resulting in 4 vol% $H_2O$ sufficient to measure a particle increase. Nevertheless, it cannot be the only driving force; otherwise, a higher Ni coarsening should be observed under the electrolysis operation. Ni coarsening and migration are concurrent effects: the Ni mobility influenced by the applied polarization shows effects on the sintering process. Under the electrolysis mode, the water content is more than 8 times higher but this operation is also characterised by higher overpotentials, which cause Ni migration to the electrode bulk hindering the particle size increase as well as partially levelling the differences between the inlet and the outlet sections. Whereas the mitigating effect of Ni migration is less emphasized under a fuel cell mode in view of its lower polarizations, as partially confirmed by a higher particle size detected at the fuel cell outlet where there are lower current densities.

Referring to the effects on the cell performance, Ni conductivity in the aged functional layer is lower due to both a bigger particle size and a smaller phase fraction that reduce the contact area among particles, penalising charge migration. The minimum value is reached at the inlet of the electrolysis working sample (~2.5 S $cm^{-1}$). In fuel cell durability tests, a bit higher values of Ni conductivity (5.3 S $cm^{-1}$ as the minimum) are detected due to the balance between a higher Ni fraction and larger Ni particles. Referring to Ni-YSZ catalytic activity, both Ni agglomeration and migration change TPB density according to the percolation theory (Table 1). Nevertheless, a lower value of the average TPB density is computed for the cell aged in electrolysis mode (1.09 $\mu m^{-2}$ SOEC vs. 1.25 $\mu m^{-2}$ SOFC), which points out Ni depletion issues. Such a reduction has a direct influence on Ni-YSZ activation overpotential [49], resulting in an absolute degradation rate of ~26 mV $kh^{-1}$ with respect to ~20 mV $kh^{-1}$ after SOFC aging (@50/50 vol% $H_2/H_2O$ fuel mixture and dry air at 750 °C).

## 5. Conclusions

Ni-YSZ cermet has a well-known catalytic activity for hydrogen evolution, yielding the perfect candidate as a solid oxide cell electrode. Nevertheless, it is also characterized by a significant instability, which becomes the source of severe performance drops during a long-term operation. Aiming at a clear identification of the working condition influence, the authors compared Ni-YSZ electrode aging under fuel cell and electrolysis mode by testing Ni-YSZ/YSZ/CGO/LSCF-CGO hydrogen electrode-supported cells for 1000 h under galvanostatic conditions at equal temperatures and current density absolute values. The experimental activity was aided by 2D modelling, which allowed local phenomenon analysis on the cell plane. Focusing here mainly on the electrolysis durability test, a cell degradation rate of ~3.5 V% $kh^{-1}$ was detected above all due to Ni-YSZ degradation, as pointed out by both EIS spectra and post-mortem microstructural analysis. Indeed, a Ni phase fraction reduction of ~50 % coupled with a particle increase of ~20 % results in a significant increase in the activation overpotential. Comparing two operations, the electrolysis working mode favours mainly Ni migration which causes its depletion within 2–5 μm close to the electrolyte interface. Whereas fuel cell aging is characterised by a more significant particle increase. Both aspects show a major effect on the catalytic activity, with a negligible worsening of the electron conductivity since the percolating network is never completely lost. According to local model results, the steam and the current density are the main accelerating factors under an almost isothermal operation. The Ni coarsening is also activated at low humidity levels, but the particle growth can be slowed down by Ni migration due to the applied overpotentials. This means a lower Ni phase fraction along with a lower particle size under electrolysis aging. Differently, fuel cell aging causes larger particles since the Ni migration hindering effect is less emphasized in view of lower local current density gradients (i.e., lower overpotentials).

## CRediT authorship contribution statement

**Aiswarya Krishnakumar Padinjarethil:** Writing – review & editing, Visualization, Validation, Investigation, Data curation, Conceptualization. **Fiammetta Rita Bianchi:** Writing – review & editing, Writing – original draft, Visualization, Validation, Software, Methodology, Data curation, Conceptualization. **Anke Hagen:** Writing – review & editing, Supervision, Funding acquisition, Conceptualization. **Barbara Bosio:** Writing – review & editing, Supervision, Funding acquisition, Conceptualization.

## Declaration of competing interest

The authors declare that they have no known competing financial interests or personal relationships that could have appeared to influence the work reported in this paper.

## Acknowledgements

Funding: This project has received funding from the Fuel Cells and Hydrogen 2 Joint Undertaking under Grant Agreement No 825027 (AD ASTRA Project). This Joint Undertaking receives support from the European Union's Horizon 2020 research and innovation programme and Hydrogen Europe.

## Appendix A. Supplementary data

Supplementary data to this article can be found online at https://doi.org/10.1016/j.jpowsour.2025.236296.

## Data availability

The data that has been used is confidential.

## References

[1] S.J. Mcphail, J. Kiviaho, B. Conti, The yellow pages of SOFC Technology, in IEA Implementing Agreement Advanced Fuel Cells Annex 32 - SOFC2017. (2017). https://www.pubblicazioni.enea.it/download.html?task=download.send&id=82:the-yellow-pages-of-sofc-technology&catid=3.

[2] P. Di Giorgio, U. Desideri, Potential of reversible solid oxide cells as electricity storage system, Energies 9 (8) (2016) 662, https://doi.org/10.3390/en9080662.

[3] M. Bertoldi, O.F. Bucheli, A. Ravagni, Development, manufacturing and deployment of SOFC-based products at SOLIDpower, ECS Trans. 78 (1) (2017) 117–123, https://doi.org/10.1149/07801.0117ecst.

[4] Bloom Units for IKEA and ASP in California, and Market in Japan, Fuel Cell. Bull. 2015 (4) (2015) 7–8, https://doi.org/10.1016/S1464-2859(15)30084-5.

[5] O. Posdziech, K. Schwarze, J. Brabandt, Efficient hydrogen production for industry and electricity storage via high-temperature electrolysis, Int. J. Hydrogen Energy 44 (35) (2019) 19089–19101, https://doi.org/10.1016/j.ijhydene.2018.05.169.

[6] J. Mermelstein, C. Cannova, M. Cruz, B. Anderson, Field demonstration of a novel reversible SOFC system for islanded microgrid energy storage, ECS Trans. 78 (1) (2017) 2907–2912, https://doi.org/10.1149/07801.2907ecst.

[7] F.R. Bianchi, B. Bosio, Operating principles, performance and technology readiness level of reversible solid oxide cells, Sustainability 13 (9) (2021) 4777, https://doi.org/10.3390/su13094777.

[8] S.J. McPhail, S. Frangini, J. Laurencin, E. Effori, A. Abaza, A.K. Padinjarethil, A. Hagen, A. Léon, A. Brisse, D. Vladikova, B. Burdin, F.R. Bianchi, B. Bosio, P. Piccardo, R. Spotorno, H. Uchida, P. Polverino, E.A. Adinolfi, F. Postiglione, J. Lee, H. Moussaoui, J. Van herle, Addressing planar solid oxide cell degradation mechanisms: a critical review of selected components, Electrochem. Sci. Adv. 2 (5) (2022), https://doi.org/10.1002/elsa.202100024.

[9] S. Nuggehalli Sampathkumar, P. Aubin, K. Couturier, X. Sun, B.R. Sudireddy, S. Diethelm, M. Pérez-Fortes, J. Van Herle, Degradation study of a reversible solid oxide cell (rSOC) short stack using distribution of relaxation times (DRT) analysis, Int. J. Hydrogen Energy 47 (18) (2022) 10175–10193, https://doi.org/10.1016/j.ijhydene.2022.01.104.

[10] Y. Liu, Z. Shao, T. Mori, S.P. Jiang, Development of nickel based cermet anode materials in solid oxide fuel cells – now and future, Mater. Rep.: Energy 1 (1) (2021) 100003, https://doi.org/10.1016/j.matre.2020.11.002.

[11] M.B. Mogensen, M. Chen, H.L. Frandsen, C. Graves, A. Hauch, P.V. Hendriksen, T. Jacobsen, S.H. Jensen, T.L. Skafte, X. Sun, Ni migration in solid oxide cell electrodes: review and revised hypothesis, Fuel Cell. (2021) 202100072, https://doi.org/10.1002/fuce.202100072 fuce.

[12] A. Faes, A. Hessler-Wyser, D. Presvytes, C.G. Vayenas, J. Van herle, Nickel-zirconia anode degradation and Triple phase boundary quantification from microstructural analysis, Fuel Cell. 10 (2) (2010), https://doi.org/10.1002/fuce.201090004, 325–325.

[13] M. Hubert, J. Laurencin, P. Cloetens, B. Morel, D. Montinaro, F. Lefebvre-Joud, Impact of nickel agglomeration on solid oxide cell operated in fuel cell and electrolysis modes, J. Power Sources 397 (2018) 240–251, https://doi.org/10.1016/j.jpowsour.2018.06.097.

[14] L. Holzer, B. Iwanschitz, Th Hocker, B. Münch, M. Prestat, D. Wiedenmann, U. Vogt, P. Holtappels, J. Sfeir, A. Mai, Th Graule, Microstructure degradation of cermet anodes for solid oxide fuel cells: quantification of nickel grain growth in dry and in humid atmospheres, J. Power Sources 196 (3) (2011) 1279–1294, https://doi.org/10.1016/j.jpowsour.2010.08.017.

[15] Z. Jiao, N. Takagi, N. Shikazono, N. Kasagi, Study on local morphological changes of nickel in solid oxide fuel cell anode using porous Ni pellet electrode, J. Power Sources 196 (3) (2011) 1019–1029, https://doi.org/10.1016/j.jpowsour.2010.08.047.

[16] M.B. Mogensen, A. Hauch, X. Sun, M. Chen, Y. Tao, S.D. Ebbesen, K.V. Hansen, P. V. Hendriksen, Relation between Ni particle shape change and Ni migration in Ni-YSZ electrodes - a hypothesis, Fuel Cell. 17 (4) (2017) 434–441, https://doi.org/10.1002/fuce.201600222.

[17] P. Moçoteguy, A. Brisse, A review and comprehensive analysis of degradation mechanisms of solid oxide electrolysis cells, Int. J. Hydrogen Energy 38 (36) (2013) 15887–15902, https://doi.org/10.1016/j.ijhydene.2013.09.045.

[18] M.Z. Khan, M.T. Mehran, R.-H. Song, J.-W. Lee, S.-B. Lee, T.-H. Lim, A simplified approach to predict performance degradation of a solid oxide fuel cell anode, J. Power Sources 391 (2018) 94–105, https://doi.org/10.1016/j.jpowsour.2018.04.080.

[19] Y. Wang, C. Wu, B. Zu, M. Han, Q. Du, M. Ni, K. Jiao, Ni migration of Ni-YSZ electrode in solid oxide electrolysis cell: an integrated model study, J. Power Sources 516 (2021) 230660, https://doi.org/10.1016/j.jpowsour.2021.230660.

[20] B. Bosio, F.R. Bianchi, Multiscale modelling potentialities for solid oxide fuel cell performance and degradation analysis, Sustain. Energy Fuels 7 (1) (2023) 280–293, https://doi.org/10.1039/D2SE01118B.

[21] D. Chen, Z. Lin, H. Zhu, R.J. Kee, Percolation theory to predict effective properties of solid oxide fuel-cell composite electrodes, J. Power Sources 191 (2) (2009) 240–252, https://doi.org/10.1016/j.jpowsour.2009.02.051.

[22] X. Sun, P.V. Hendriksen, M.B. Mogensen, M. Chen, Degradation in solid oxide electrolysis cells during long term testing, Fuel Cell. 19 (6) (2019) 740–747, https://doi.org/10.1002/fuce.201900081.

[23] M. Trini, A. Hauch, S. De Angelis, X. Tong, P.V. Hendriksen, M. Chen, Comparison of microstructural evolution of fuel electrodes in solid oxide fuel cells and electrolysis cells, J. Power Sources 450 (2020) 227599, https://doi.org/10.1016/j.jpowsour.2019.227599.

[24] A. Nakajo, G. Rinaldi, P. Caliandro, G. Jeanmonod, L. Navratilova, M. Cantoni, J. Van Herle, Evolution of the morphology near triple-phase boundaries in Ni–yttria stabilized Zirconia electrodes upon cathodic polarization, J. Electrochem. Energy Conv. Storage 17 (4) (2020) 041004, https://doi.org/10.1115/1.4046478.

[25] A. Hauch, K. Brodersen, M. Chen, M.B. Mogensen, Ni/YSZ electrodes structures optimized for increased electrolysis performance and durability, Solid State Ionics 293 (2016) 27–36, https://doi.org/10.1016/j.ssi.2016.06.003.

[26] A.K. Padinjarethil, F.R. Bianchi, B. Bosio, A. Hagen, Electrochemical characterization and modelling of anode and electrolyte supported solid oxide fuel cells, Front. Energy Res. 9 (2021) 668964, https://doi.org/10.3389/fenrg.2021.668964.

[27] F.R. Bianchi, A.K. Padinjarethil, A. Hagen, B. Bosio, Multiscale analysis of Ni-YSZ and Ni-CGO anode based SOFC degradation: from local microstructural variation to cell electrochemical performance, Electrochim. Acta 460 (2023) 142589, https://doi.org/10.1016/j.electacta.2023.142589.

[28] A.K. Padinjarethil, F.R. Bianchi, B. Bosio, A. Hagen, Degradation of Ni-YSZ and Ni-GDC fuel cells after 1000 h operation: analysis of different overpotential contributions according to electrochemical and microstructural characterization, E3S Web Conf. 334 (2022) 04011, https://doi.org/10.1051/e3sconf/202233404011.

[29] D. Bove, E. Audasso, T. Barckholtz, G. Kiss, J. Rosen, B. Bosio, Process analysis of molten carbonate fuel cells in carbon capture applications, Int. J. Hydrogen Energy 46 (28) (2021) 15032–15045, https://doi.org/10.1016/j.ijhydene.2020.08.020.

[30] E. Audasso, B. Bosio, D. Bove, E. Arato, T. Barckholtz, G. Kiss, J. Rosen, H. Elsen, R. Blanco Gutierrez, L. Han, T. Geary, C. Willman, A. Hilmi, C.Y. Yuh, H. Ghezel-Ayagh, The effects of gas diffusion in molten carbonate fuel cells working as carbon capture devices, J. Electrochem. Soc. 167 (11) (2020) 114515, https://doi.org/10.1149/1945-7111/aba8b6.

[31] F.R. Bianchi, R. Spotorno, P. Piccardo, B. Bosio, Solid oxide fuel cell performance analysis through local modelling, Catalysts 10 (5) (2020) 519, https://doi.org/10.3390/catal10050519.

[32] T.A. Barckholtz, H. Elsen, P.H. Kalamaras, G. Kiss, J. Rosen, D. Bove, E. Audasso, B. Bosio, Experimental and modeling investigation of $CO^{3=}/OH^{-}$ equilibrium effects on molten carbonate fuel cell performance in carbon capture applications, Front. Energy Res. 9 (2021) 669761, https://doi.org/10.3389/fenrg.2021.669761.

[33] A. Hauch, A. Ploner, S. Pylypko, G. Cubizolles, J. Mougin, Test and characterization of reversible solid oxide cells and stacks for innovative renewable energy storage, Fuel Cell. (2021) 202100046, https://doi.org/10.1002/fuce.202100046 fuce.

[34] D. Chen, W. Bi, W. Kong, Z. Lin, Combined micro-scale and macro-scale modeling of the composite electrode of a solid oxide fuel cell, J. Power Sources 195 (19) (2010) 6598–6610, https://doi.org/10.1016/j.jpowsour.2010.04.065.

[35] F.R. Bianchi, B. Bosio, A. Baldinelli, L. Barelli, Optimization of a reference kinetic model for solid oxide fuel cells, Catalysts 10 (1) (2020) 104, https://doi.org/10.3390/catal10010104.

[36] F.R. Bianchi, A. Baldinelli, L. Barelli, G. Cinti, E. Audasso, B. Bosio, Multiscale modeling for reversible solid oxide cell operation, Energies 13 (19) (2020) 5058, https://doi.org/10.3390/en13195058.

[37] T. Skafte, J. Hjelm, P. Blennow, C. Graves, Quantitative review of degradation and lifetime of solid oxide cells and stacks **2016**, in: Proceedings of 12th European SOFC & SOE Forum, 2016, pp. 8–27. Article B0501 European Fuel Cell Forum. Available online: https://orbit.dtu.dk/en/publications/quantitative-review-of-degradation-and-lifetime-of-solid-oxide-ce(12/08/2024.

[38] Y. Yang, X. Tong, A. Hauch, X. Sun, Z. Yang, S. Peng, M. Chen, Study of solid oxide electrolysis cells operated in potentiostatic mode: effect of operating temperature on durability, Chem. Eng. J. 417 (2021) 129260, https://doi.org/10.1016/j.cej.2021.129260.

[39] S.E. Wolf, V. Vibhu, E. Tröster, I.C. Vinke, R.-A. Eichel, L.G.J. (Bert) de Haart, Steam electrolysis vs. Co-electrolysis: mechanistic studies of long-term solid oxide lectrolysis cells, Energies 15 (15) (2022) 5449, https://doi.org/10.3390/en15155449.

[40] A. Hauch, S. Pylypko, G. Cubizolles, J. Mouginn, Load cycling tests of reversible solid oxide cells – effects of current density, steam content, and utilization, ECS Trans. 103 (1) (2021) 437–450, https://doi.org/10.1149/10301.0437ecst.

[41] X. Tong, P.V. Hendriksen, A. Hauch, X. Sun, M. Chen, An up-scalable, infiltration-based approach for improving the durability of Ni/YSZ electrodes for solid oxide cells, J. Electrochem. Soc. 167 (2) (2020) 024519, https://doi.org/10.1149/1945-7111/ab6f5c.

[42] A. Leonide, SOFC Modelling and Parameter Identification by Means of Impedance Spectroscopy, KIT Scientific Publishing, Karlsruhe, 2010. Available online: https://publikationen.bibliothek.kit.edu/1000019173(12/08/2024.

[43] M. Rao, S.H. Jensen, X. Sun, A. Hagen, Unwinding entangled degradation mechanisms in solid oxide electrolysis cells through electrode modifications and impedance analysis, Fuel Cell. (2019) 201800166, https://doi.org/10.1002/fuce.201800166 fuce.

[44] M. Rao, X. Sun, A. Hagen, A comparative study of durability of solid oxide electrolysis cells tested for Co-electrolysis under galvanostatic and potentiostatic conditions, J. Electrochem. Soc. 165 (10) (2018) F748–F755, https://doi.org/10.1149/2.0151810jes.

[45] J. Laurencin, M. Hubert, D.F. Sanchez, S. Pylypko, M. Morales, A. Morata, B. Morel, D. Montinaro, F. Lefebvre-Joud, E. Siebert, Degradation mechanism of $La_{0.6}Sr_{0.4}Co_{0.2}Fe_{0.8}O_{3-\delta}/Gd_{0.1}Ce_{0.9}O_{2-\delta}$ composite electrode operated under solid oxide electrolysis and fuel cell conditions, Electrochim. Acta 241 (2017) 459–476, https://doi.org/10.1016/j.electacta.2017.05.011.

[46] M.Z. Khan, M.T. Mehran, R.-H. Song, S.-B. Lee, T.-H. Lim, Effects of applied current density and thermal cycling on the degradation of a solid oxide fuel cell cathode, Int. J. Hydrogen Energy 43 (27) (2018) 12346–12357, https://doi.org/10.1016/j.ijhydene.2018.04.175.

[47] C.E. Frey, Q. Fang, D. Sebold, L. Blum, N.H. Menzler, A detailed post mortem analysis of solid oxide electrolyzer cells after long-term stack operation, J. Electrochem. Soc. 165 (5) (2018) F357–F364, https://doi.org/10.1149/2.0961805jes.

[48] Y. Chen, S. Yoo, X. Li, D. Ding, K. Pei, D. Chen, Y. Ding, B. Zhao, R. Murphy, B. deGlee, J. Liu, M. Liu, An effective strategy to enhancing tolerance to contaminants poisoning of solid oxide fuel cell cathodes, Nano Energy 47 (2018) 474–480, https://doi.org/10.1016/j.nanoen.2018.03.043.
[49] F. Monaco, M. Hubert, J. Vulliet, D. Montinaro, J.P. Ouweltjes, P. Cloetens, P. Piccardo, F. Lefebvre-Joud, J. Laurencin, Impact of microstructure and polarization on the degradation of Ni-YSZ electrode: an experimental and modeling approach, ECS Trans. 91 (1) (2019) 653–664, https://doi.org/10.1149/09101.0653ecst.
[50] Q. Fang, L. Blum, N.H. Menzler, Performance and degradation of solid oxide electrolysis cells in stack, J. Electrochem. Soc. 162 (8) (2015) F907–F912, https://doi.org/10.1149/2.0941508jes.
[51] J. Bowen, ManSeg. MATLAB central file exchange, Available online: https://www.mathworks.com/matlabcentral/fileexchange/75347-manseg. (Accessed 11 January 2022).
[52] C.A. Schneider, W.S. Rasband, K.W. Eliceiri, NIH image to ImageJ: 25 Years of image analysis, Nat. Methods 9 (7) (2012) 671–675, https://doi.org/10.1038/nmeth.2089.
[53] F. Zabihian, A.S. Fung, Macro-level modeling of solid oxide fuel cells, approaches, and assumptions revisited, J. Renew. Sustain. Energy 9 (5) (2017) 054301, https://doi.org/10.1063/1.5006909.
[54] T. Yonekura, Y. Tachikawa, T. Yoshizumi, Y. Shiratori, K. Ito, K. Sasaki, Exchange current density of solid oxide fuel cell electrodes, ECS Trans. 35 (1) (2019) 1007–1014, https://doi.org/10.1149/1.3570081.
[55] E. Effori, J. Laurencin, E.D.R. Silva, M. Hubert, T. David, M. Petitjean, G. Geneste, L. Dessemond, E. Siebert, An elementary kinetic model for the LSCF and LSCF-CGO electrodes of solid oxide cells: impact of operating conditions and degradation on the electrode response, J. Electrochem. Soc. 168 (4) (2021) 044520, https://doi.org/10.1149/1945-7111/abf40a.
[56] B. Conti, B. Bosio, S.J. McPhail, F. Santoni, D. Pumiglia, E. Arato, A 2-D model for intermediate temperature solid oxide fuel cells preliminarily validated on local values, Catalysts 9 (1) (2019) 36, https://doi.org/10.3390/catal9010036.
[57] F. Monaco, M. Hubert, J. Vulliet, J.P. Ouweltjes, D. Montinaro, P. Cloetens, P. Piccardo, F. Lefebvre-Joud, J. Laurencin, Degradation of Ni-YSZ electrodes in solid oxide cells: impact of polarization and initial microstructure on the Ni evolution, J. Electrochem. Soc. 166 (15) (2019) F1229–F1242, https://doi.org/10.1149/2.1261915jes.
[58] D.A. Noren, M.A. Hoffman, Clarifying the butler–volmer equation and related approximations for calculating activation losses in solid oxide fuel cell models, J. Power Sources 152 (2005) 175–181, https://doi.org/10.1016/j.jpowsour.2005.03.174.
[59] N.H. Menzler, D. Sebold, Y.J. Sohn, S. Zischke, Post-test characterization of a solid oxide fuel cell after more than 10 Years of stack testing, J. Power Sources 478 (2020) 228770, https://doi.org/10.1016/j.jpowsour.2020.228770.
[60] L. Rorato, Y. Shang, S. Yang, M. Hubert, K. Couturier, L. Zhang, J. Vulliet, M. Chen, J. Laurencin, Understanding the Ni migration in solid oxide cell: a coupled experimental and modeling approach, J. Electrochem. Soc. 170 (3) (2023) 034504, https://doi.org/10.1149/1945-7111/acc1a3.
[61] R. Knibbe, M.L. Traulsen, A. Hauch, S.D. Ebbesen, M. Mogensen, Solid oxide electrolysis cells: degradation at high current densities, J. Electrochem. Soc. 157 (8) (2010) B1209, https://doi.org/10.1149/1.3447752.
[62] M. Chen, Y.-L. Liu, J.J. Bentzen, W. Zhang, X. Sun, A. Hauch, Y. Tao, J.R. Bowen, P. V. Hendriksen, Microstructural degradation of Ni/YSZ electrodes in solid oxide electrolysis cells under high current, J. Electrochem. Soc. 160 (8) (2013) F883–F891, https://doi.org/10.1149/2.098308jes.
[63] V. Bilalis, X. Sun, H.L. Frandsen, M. Chen, Quantifying galvanostatic degradation of solid oxide electrolysis cells: the onset of accelerated degradation of Ni-yttria stabilized Zirconia electrode, J. Power Sources 606 (2024) 234490, https://doi.org/10.1016/j.jpowsour.2024.234490.
[64] S. Gao, J. Li, Z. Lin, Theoretical model for surface diffusion driven Ni-particle agglomeration in anode of solid oxide fuel cell, J. Power Sources 255 (2014) 144–150, https://doi.org/10.1016/j.jpowsour.2014.01.033.
[65] B. Königshofer, M. Höber, G. Nusev, P. Boškoski, C. Hochenauer, V. Subotić, Accelerated degradation for solid oxide electrolysers: analysis and prediction of performance for varying operating environments, J. Power Sources 523 (2022) 230982, https://doi.org/10.1016/j.jpowsour.2022.230982.